IEEE Access
Multidisciplinary | Rapid Review | Open Access Journal

Received April 8, 2021, accepted April 21, 2021, date of publication April 28, 2021, date of current version May 6, 2021.

Digital Object Identifier 10.1109/ACCESS.2021.3076343

Transition Flight Control and Simulation of a Novel Tail-Sitter UAV With Varying Fuselage Shape

XINGLU XIA[1], MUQING YANG[1], GANG CHEN[1], LIANG ZHANG[1], AND JIAJIA HOU[2]
[1]School of Aeronautic Science and Engineering, Beihang University, Beijing 100191, China
[2]Science and Technology on Space Physics Laboratory, Beijing 100076, China

Corresponding author: Muqing Yang (qingfengrumu@163.com)

ABSTRACT This article studies the model, control and simulation on transition flight of a novel tail-sitter with vertical takeoff and landing capability. The proposed tail-sitter adopts an innovative varying fuselage shape design to break the technical bottleneck in the balance of efficient horizontal flight and agile vertical flight. Overset grids and computational fluid dynamic methods are used to explore the vehicle's prestall aerodynamics, which are relative to not only the angle of attack and sideslip angle but also to the varying angle between two rear fuselage's parts. High angle of attack aerodynamics based on the improved Viterna and Corrigan stall model is also established for this novel tail-sitter. Meanwhile, an accurate model of the propeller is tested in a wind tunnel. Combining the forces and moments generated by propellers, aerodynamics and gravity, a 6DoF nonlinear time-varying dynamic model is built. A robust controller based on incremental dynamic inversion method is designed for this tail-sitter, which is good at dealing with uncertainties and external forces. Nominal and model mismatch conditions are simulated to verify the controller's performance. Different varying strategies for the mechanism are analyzed during the transition flight. Simulation results show that this novel tail-sitter can transform between vertical and horizontal flight mode easily and the varying strategy related to pitch angle is a prior choice for transition flight.

INDEX TERMS Novel tail-sitter, varying fuselage shape, transition flight, incremental nonlinear inversion method, vertical takeoff and landing.

I. INTRODUCTION

Unmanned aerial vehicle (UAV) technology has developed rapidly and been applied in various fields such as photography, cargo delivery, environmental observation, etc. Reference [1], [2] combining the long endurance and high speed of the fixed-wing and vertical take-off and landing (VTOL) ability of rotorcraft, hybrid type UAVs have attracted a lot of attention in recent years. Reference [3]–[7] hybrid UAVs include a variety of types such as tail-sitter, tilt-wing, tilt-rotor and rotary wing [8]. Among them, the tail-sitter has been a hot spot due to its simple design. Over the UAVs assisted with a launcher [9], the tail-sitter has the advantages of convenience and fast takeoff and landing ability. However, compared to the tilt wing or tilt rotors, most of tail-sitters are less controllable in pitch motion during low-speed flight conditions, for example the early stage of the forward transition flight. This is because a considerable quantity of tail-sitters' pitching control depends on the flaps immersed in the propellers' slipstream like T-wing [10] and VD200 [11], which are less effective when the propeller has a relative low disc loading [12] or when the vehicle is descending. There is also a number of tail-sitters' pitching control depends on the propellers mounted on the tip of vertical tails or short supporting rods such as ATMOS [13] and VertiKUL [14], which have shorter pitching control arms than that of tilt-wings. Meanwhile, due to the short distance between the center of gravity and elevons, the fly-wing configuration usually used in tail-sitter is less maneuverable in pitch motion during cruise flight than a conventional configuration [15]. Therefore, a novel tail-sitter with varying fuselage shape is proposed in this article to break the technical bottleneck in the balance of efficient horizontal flight and agile vertical flight.

Accurate dynamic model is necessary for the control and simulation of this novel tail-sitter. Computational fluid method (CFD) is a general accurate and reliable way to simulate the air flow. However, for the high angle of attack (AOA) flow with separation, CFD method costs more

The associate editor coordinating the review of this manuscript and approving it for publication was Jiankang Zhang.

time and resource. Ref. [16] used a model for nonrotating finite-length rectangular wings to simulate the tiltwing's high AOA aerodynamics and applied it to the trajectory optimization. The model is developed by Tangler and Ostowari [17] based on experiments and the model of Viterna and Corrigan [18]. It is easy to be used only requiring the 2D foil aerodynamics, aspect ratio (AR) and stall angle for a wing.

The varying of fuselage shape leads to the large changes of moments of inertia, causing the novel tail-sitter to be a time-varying system during the transition flight. Multi-body dynamic modeling method can capture all the motion of every component precisely and has been used in tilt-rotors [19] and tilt-wings [20] successfully. But when the influences of every component's relative motion are able to be modelled accurately, it is obviously easier to treat the vehicle as a whole [21]. The influences mentioned above include those on the aerodynamics, center of gravity, control effectiveness, moments of inertia, etc.

A safe transition flight is necessary for the hybrid UAV. During this process, the pitch angle's variation is close to 90°, which results in strong nonlinearity of the dynamic model and difficulty in controller design. Conventional rotation matrix with Yaw-Pitch-Roll order is singular when the pitch angle is 90°. Using the Yaw-Roll-Pitch order rotation matrix can solve this problem easily and it is simple to understand [22]. As for the control problem for tail-sitter, variety of controllers are studied by different researchers. PID controller is a common choice in real applications which does not need the knowledge of tail-sitter model [14], [23], [24]. LQR controller scheme [25] can handle multi-input multi-output (MIMO) system easily but require the full state information which is not always possible. Gain-Scheduling controller is a good choice for full flight control but has a relative high cost for computation [26], [27]. Nonlinear dynamic inversion (NDI) method has gained a lot of attention for its simplicity to be tuned [8], [28]. The main restriction on its wide application is that precise knowledge of the dynamic model is required. One option to reduce sensitivity to model errors is incremental nonlinear dynamic inversion (INDI) [29]–[32], which uses the estimations of the acceleration from sensor data to replace the dynamics model. Many researches have tried to using INDI based controller in the transition flight control of hybrid UAVs. For example, a robust transition controller for a fly-wing tail-sitter based on INDI is designed to deal with model uncertainties and validated by simulations under a variety of conditions [32]. In another study [31], multiple outdoor experiments were performed to validate the incremental control structure's effectiveness on compensating unmodeled forces and moments for a tail-sitter. Besides, two kinds of novel hybrid UAVs also used the INDI based control structure to complete the transition flight and verified its effectiveness [29], [30]. Based on the established dynamic model, we use the INDI controller for the attitude control of the UAV and conventional PID controller for the altitude control to validate the vehicle's transition flight capability.

The main contribution of this article is the validation of a novel tail-sitter UAV's transition flight capability and the effectiveness of modelling and controlling methods used on it. The structure of this article is organized as follow: The second part is an introduction to the design parameters of the novel tail-sitter and the transition flight process. The operation of the varying mechanism during the transition flight will also be introduced here. The third part is the dynamic model of the tail-sitter including coordinates, moments of inertia, propeller's performance and the whole aerodynamic model considering the high AOA conditions. Then a 6-degree-of-freedom (6DoF) dynamic model structure is constructed for the novel tail-sitter. INDI controller is designed in the fourth part. Transition flight simulations under nominal condition, model mismatch conditions and gust disturbance condition are described and analyzed in the fifth part. Different varying strategies for the rear fuselage's parts are simulated and compared here in order to get an optimal one for reliable transition flight. Finally, the last is the conclusion part of this article.

II. OBJECT DESCRIPTION

The novel tail-sitter with varying fuselage shape in this article contains four brushless motors and four propellers (denoted as P1, P2, P3 and P4) as the propulsion systems (shown in Fig.1). The spin directions and arrangement of the four propellers are shown as Fig.1(a). The fuselage is divided into three parts: one front part denoted as FP1 and two rear parts denoted as RP1 and RP2. In vertical flight mode, RP1 and RP2 are separated to an angle of 150° and locked, turning the tail-sitter into a ''plus'' style quadrotor. Compared to the existing tail-sitters such as ATMOS and VertiKUL mentioned above, the quadrotor has a relative much longer pitch control arm, which means more maneuverable and gust resistant during the vertical flight. In the horizontal flight mode (shown as Fig.1(b)), RP1 and RP2 are combined tightly and locked, turning this tail-sitter into a conventional fixed-wing UAV with medium aspect ratio (AR). Meanwhile, P1 and P3 stop rotating and are folded to reduce drag while P2 and P4 are still working to provide the power for level flight.

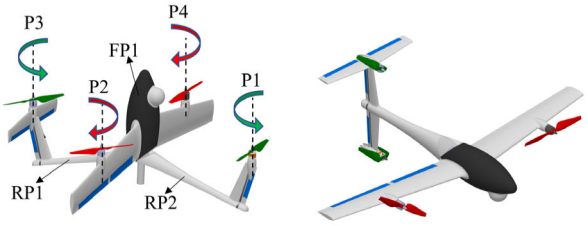

(a) Vertical flight mode (b) Horizontal flight mode

FIGURE 1. The novel tail-sitter UAV.

The forward and back transition maneuvers between vertical and horizontal flight modes are shown as Fig.2 and Fig.3.

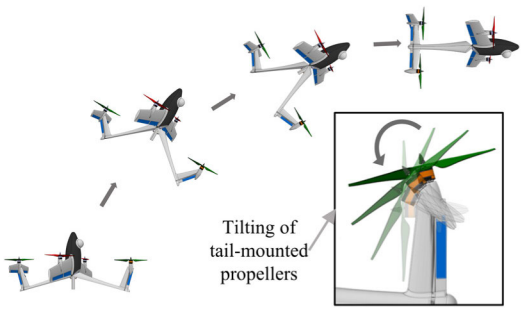

FIGURE 2. Vertical to horizontal flight transition (forward transition flight).

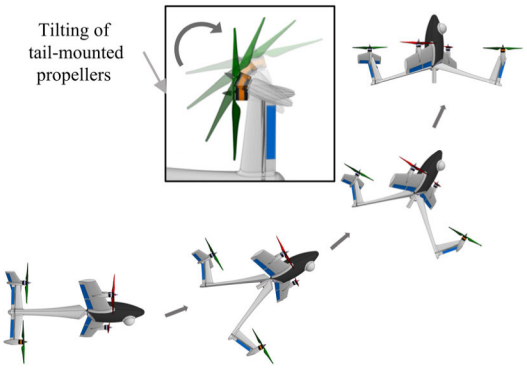

FIGURE 3. Horizontal to vertical flight transition (back transition flight).

It should be noted that when the angle between RP1 and RP2 changes between 0-150°, propellers P1 and P3 are also rotating around a corresponding axis inside the vertical tails at the same time. The axial directions of P1 and P3 are controlled to be consistent with those of P2 and P4. The driving mechanism for the rotation of RP1 and RP2 is a spiral screw, which has a large gear ratio and can realize self-lock under non-rotation condition. The drivers for P1 and P3's tilting motion is a linear servo, which has a small size to be easily contained inside the vertical tail. Flexible skin made by carbon fiber is used to fill the gap between FP1 and RP1(2) to ensure a smooth shape during horizontal flight. The design parameters of researched tail-sitter are shown as Table 1 and Fig.4.

TABLE 1. Design parameters of researched tail-sitter.

Parameters	Value	Parameters	Value
Weight	12.06kg	Airfoil	GAW-1
Cruise Speed	27.2m/s	Varying Angle σ	0~150°
Aspect Ratio (AR)	12	Sweep Back Angle $\Lambda_{1/4}$	10°
Wing Area	0.288m^2	Wing Loading	407.8N/m2
Spanwise	1.86m	Mean Aerodynamic Chord	0.155m
L_{long}	0.68m	L_{lat}	0.51m
Mechanism weight	1.95kg	ϑ	23.3°

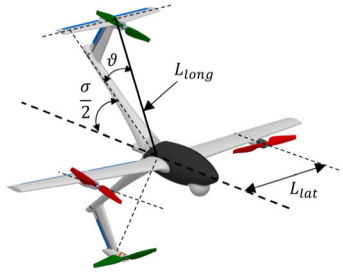

FIGURE 4. Key parameters and propellers' configuration.

Rotating mechanism for RP1 and RP2 is a trapezoid sliding lead screw with nut which is driven by a high-torque stepper motor. The nut connects two conrods which connect RP1 and RP2 separately as shown in Fig.5. Then the rotation of RP1 and RP2 can be realized by moving the screw nut back and forward along the screw rotation axis. Sliding screw can realize self-lock when the screw stops rotating and the torque of the mechanism will not be transmitted to the stepper motor under non-varying conditions. Meanwhile, stepper motor's current can be reduced to about zero during this condition to save energy.

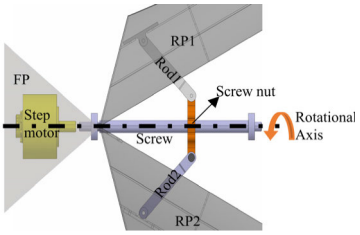

FIGURE 5. Components of fuselage shape's varying mechanism.

The specific mechanism used for tail-mounted propellers' tilting motion is shown in Fig 6. When the length of line segment *bc* is increased or decreased by the linear servo, the tail-mounted propeller will rotate around point *a* anti-clockwise or clockwise to keep the same axial direction as that of propellers ahead of wing.

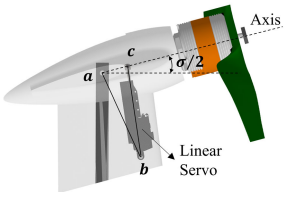

FIGURE 6. Tilting mechanism on the tail.

III. MATHEMATICAL AND PHYSICAL MODEL

A. COORDINATES AND ROTATION MATRIX

In order to control the attitude in two flight modes using one single controller, a singularity-free expression method for attitude is necessary. The Euler angles representation method with common Yaw-Pitch-Roll rotation order is singular (Gimbal Lock [22]) when the pitch angle is equal

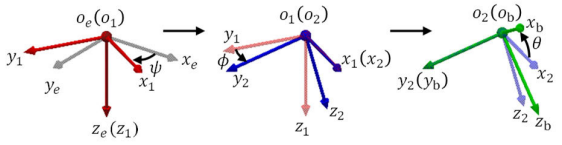

FIGURE 7. Definition of Euler angles with Yaw-Roll-Pitch rotation order.

to 90°, which is not suitable for the tail-sitter 's transition flight. Therefore, Yaw-Roll-Pitch sequence rotation matrix is adopted to represent the attitude.

As shown in Fig.7, the inertial coordinate frame is transformed to the body coordinate frame after three rotations using the Yaw-Roll-Pitch order. Rotation matrix for transforming the inertial coordinate frame to the body coordinate frame is expressed as

$$R_{be} = \begin{bmatrix} c\theta c\psi - s\phi s\theta s\psi & c\theta s\psi + s\phi s\theta c\psi & -c\phi s\theta \\ -c\phi s\psi & c\phi c\psi & s\phi \\ s\theta c\psi + s\phi c\theta s\psi & s\theta s\psi - s\phi c\theta c\psi & c\phi c\theta \end{bmatrix} \quad (1)$$

where c represents cos and s represents sin for simplicity.

Denote the angular velocity vector in the body coordinate frame as $\omega_b = \begin{bmatrix} p & q & r \end{bmatrix}^T$ and the Euler angular velocity as $\begin{bmatrix} \dot{\phi} & \dot{\theta} & \dot{\psi} \end{bmatrix}^T$, the relationship between them is

$$\begin{bmatrix} \dot{\phi} \\ \dot{\theta} \\ \dot{\psi} \end{bmatrix} = T_\eta \begin{bmatrix} p \\ q \\ r \end{bmatrix} \quad (2)$$

Here,

$$T_\eta = \begin{bmatrix} \cos\theta & 0 & \sin\theta \\ \sin\theta\tan\phi & 1 & -\cos\theta\tan\phi \\ -\sin\theta\sec\phi & 0 & \cos\theta\sec\phi \end{bmatrix} \quad (3)$$

The body and inertial coordinate frames attached to the tail-sitter in different flight modes are shown in Fig.8.

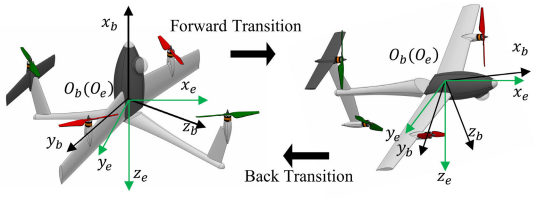

FIGURE 8. Body and inertial coordinate frames on the UAV.

B. INERTIA TENSOR

The inertia tensor of the whole tail-sitter changes with the rotation of RP1 and RP2, which has a great impact on the longitudinal stability and maneuverability of the tail-sitter. We estimated the vehicle's weight distribution under different varying angles through measuring a detailed 3-dimensional CAD model.

During the rotation of RP1 and RP2, the UAV still maintains a symmetrical configuration about the $x_b z_b$-plane, which means $I_{xy} = 0$. Meanwhile, two other products of inertia are much smaller compared to the principle moments of inertia and ignored in this article, i.e. $I_{yz} \approx 0, I_{zx} \approx 0$. The inertia tensor of the researched tail-sitter can be expressed as follow by using three cubic polynomials, which can be seen as follow.

$$\mathbf{I} = \begin{bmatrix} \sum_{i=0}^{3} X_i \sigma^i & 0 & 0 \\ 0 & \sum_{i=0}^{3} Y_i \sigma^i{}_0 & 0 \\ 0 & 0 & \sum_{i=0}^{3} Z_i \sigma^i \end{bmatrix} \quad (4)$$

Here, X_i, Y_i and Z_i represent polynomial coefficients and σ is rear fuselages' varying angle. Relationships between the principal moments of inertia and σ are shown in Fig.9(a). I_{xx}, I_{yy} and I_{zz} in vertical flight mode when $\sigma = 150°$ are different by 122.7%, −17.22% and −57.7% from those in the horizontal flight mode when $\sigma = 0°$. With the increasing of σ, the distance between the tail propulsion and x_b axis becomes larger, which leads to I_{xx}'s increasing. Fortunately, the increase of σ lengthens the pitch control arm and decreases I_{yy} at the same time, both making the tail-sitter more controllable for pitch motion in vertical flight mode. It is of great benefit to low-speed flight conditions and validates the advantages of the varying fuselage shape design. The varying motion of fuselage shape will also cause the shift of

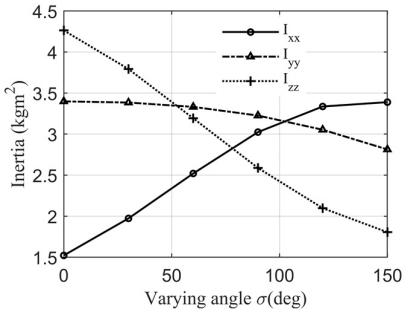

(a) Principal moments of inertia

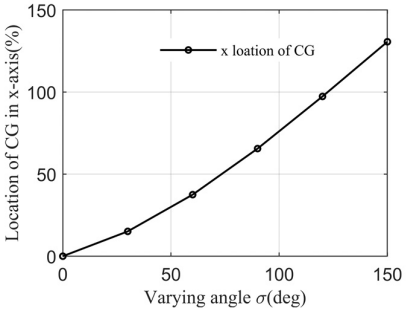

(b) Ratio between the x location of CG and mean aerodynamic chord

FIGURE 9. The influence of fuselage shape's varying motion on the principal moments of inertia and location of CG.

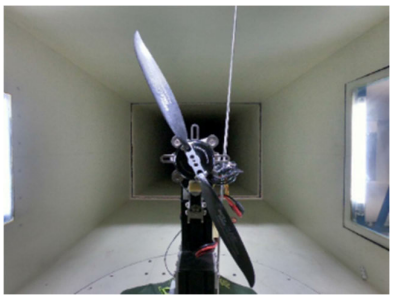

FIGURE 10. CAM 15 × 8 propeller wind tunnel test.

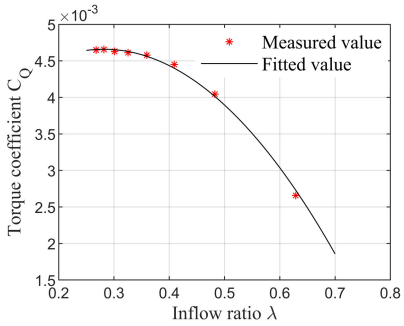

(a) Torque coefficient

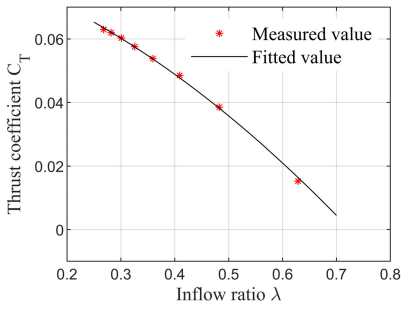

(b) Thrust coefficient

FIGURE 11. Propeller's thrust and torque coefficients test results.

center of gravity (CG), especially the location in the x-axis shown as Fig.9(b), which should be considered carefully in the external moments calculating process.

C. MOTORS AND PROPELLERS

The motor used can be represented by a continuous first-order transfer function:

$$n_i = \frac{n_{ci}}{\tau s + 1} \tag{5}$$

where τ is the time constant, n_i is real rotation speed of each motor, and n_{ci} denotes each motor's rotation speed command. The range of motor's rotation speed is $[0rps, 117rps]$.

The four propellers used are all CAM 15 × 8 and its thrust and torque are expressed as

$$\begin{cases} T_i = \rho n_i^2 D_p^4 C_{Ti} \\ Q_i = \rho n_i^2 D_p^5 C_{Qi} \end{cases} \tag{6}$$

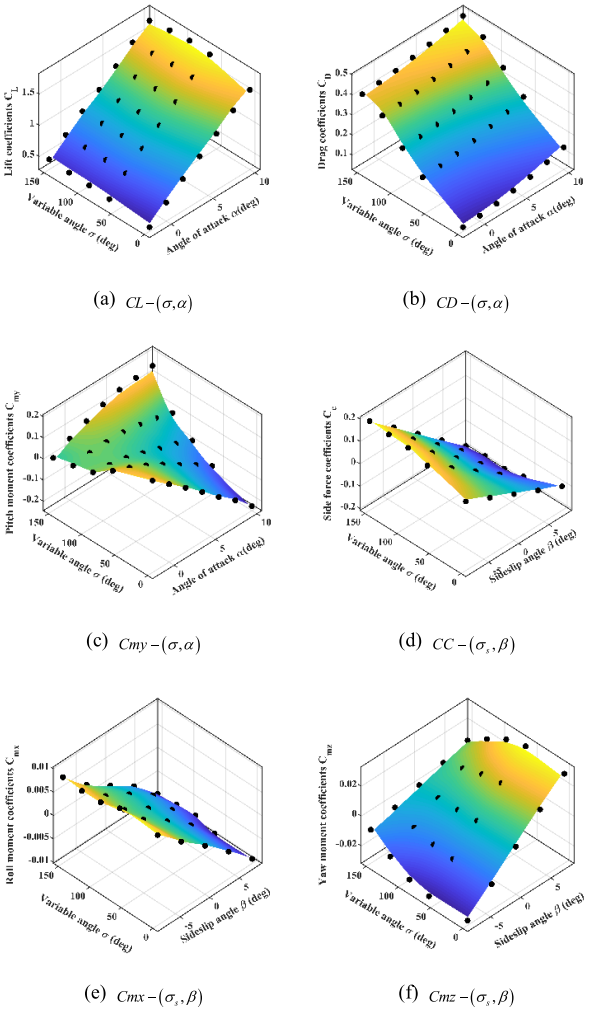

(a) $CL-(\sigma,\alpha)$ (b) $CD-(\sigma,\alpha)$

(c) $Cmy-(\sigma,\alpha)$ (d) $CC-(\sigma_s,\beta)$

(e) $Cmx-(\sigma_s,\beta)$ (f) $Cmz-(\sigma_s,\beta)$

FIGURE 12. Prestall aerodynamics of researched tail-sitter.

where D_P is the propeller's diameter, C_{Ti} and C_{Qi} are the thrust and torque coefficients. We conducted a wind tunnel test to obtain the relationships between the coefficients and the advance ratio. Two quadratic polynomial curves are used to fit the test data in this article.

$$\begin{cases} C_{Ti} = P_{T0} + P_{T1}\lambda_i + P_{T2}\lambda_i^2 \\ C_{Qi} = P_{Q0} + P_{Q1}\lambda_i + P_{Q2}\lambda_i^2 \end{cases} \tag{7}$$

Here, the advance ratio is calculated by $\lambda_i = V_\perp / (n_i D_P)$ and $V_\perp$ denotes advance velocity, i.e. the axial inflow velocity for each propeller.

D. AERODYNAMICS

1) PRESTALL AERODYNAMICS

Fuselage shape's varying motion has a significant impact on the aerodynamics of the tail-sitter. Using overset-grid and computational fluid dynamic (CFD) methods, we calculated the aerodynamic coefficients of the tail-sitter before stall. The results are shown as Fig.13.

It can be seen that the rear fuselage's opening increases the drag for the growing of fuselage's windward area. The slope of $C_{my} - \alpha$ is also changed largely by the varying distance between the CG and horizontal tail. Using polynomial and trigonometric hybrid curve fitting method, the prestall static longitudinal aerodynamics of the whole tail-sitter is given by

$$\begin{aligned} C_L &= C_{L0} + C_{L\alpha}\alpha + C_{L\sigma}\sigma \\ C_D &= C_2\alpha^2 + C_1\alpha + C_0 + S_1\cos(\sigma + \sigma_0) \\ C_{my} &= C_{my0} + C_{my\alpha}\alpha + C_{my\sigma 1}\sigma + C_{my\alpha\sigma}\alpha\sigma + C_{my\sigma 2}\sigma^2 \end{aligned} \tag{8}$$

Lateral aerodynamics of the UAV is also given by

$$\begin{aligned} C_C &= C_{C\beta}\beta + C_{C\beta\sigma}\beta\sigma \\ C_{mx} &= C_{mx\beta}\beta + C_{mx\beta\sigma}\beta\sigma \\ C_{mz} &= C_{mz\beta}\beta + C_{mz\beta\sigma}\beta\sigma \end{aligned} \tag{9}$$

In (8) and (9), C_L, C_D, C_C represent the lift, drag and side force coefficients in the wind coordinate. C_{mx}, C_{my}, C_{mz} are the moments coefficients around three body axes. α, β, σ are AOA, sideslip angle and angle between RP1 and RP2. $C_{L0}, C_{L\alpha}, C_{L\sigma}, C_2, C_1, C_0, S_1, \sigma_0, C_{my0}, C_{my\alpha}$, $C_{my\sigma 1}, C_{my\alpha\sigma}, C_{my\sigma 2}$ are all known fitted parameters.

2) HIGH ANGLE OF ATTACK AERODYNAMIC

The tail-sitter will experience a high angle of attack state with large uncertainties during the altitude-hold transition flight. We use a model developed by Tangler and Ostowar [17] for nonrotating finite-length wings based on experimental data and the model of Viterna and Corrigan. Reference [18] Some researchers have applied this method to the study of the optimization of tilt-wing's take-off trajectory [5], which validated the model's adaption on the vertical take-off and landing aerial vehicles.

The poststall lift coefficient is given by

$$C_L = A_1 \sin 2\alpha + A_2 \frac{\cos^2\alpha}{\sin\alpha} \tag{10}$$

where

$$\begin{aligned} A_1 &= \frac{C_1}{2} \\ A_2 &= \left(C_{L_s} - C_1 \sin\alpha_s \cos\alpha_s\right) \frac{\sin\alpha_s}{\cos^2\alpha_s} \\ C_1 &= 1.1 + 0.018AR \end{aligned}$$

Here, α_s is the AOA at stall, C_{Ls} is the lift coefficient at stall, and AR is the aspect ratio of the wing.

The poststall drag coefficient is given by

$$C_D = B_1 \sin\alpha + B_2 \cos\alpha \tag{11}$$

where

$$\begin{aligned} B_1 &= C_{D_{\max}} \\ B_2 &= \frac{C_{D_s} - C_{D_s}\sin\alpha_s}{\cos\alpha_s} \\ C_{D_{\max}} &= \frac{1.0 + 0.065AR}{0.9 + t/c} \end{aligned}$$

Here, C_{D_s} is the drag coefficient at stall, t/c is the relative thickness of the used airfoi. The CFD simulation calculation shows that the stall angle of attack of the wing is about 15°.

Cubic polynomials are used for combining the prestall and poststall longitudinal aerodynamic curves and they are first-order continuous at the connecting AOA. As a result, the lift, drag and pitch moment curves of the studied tail-sitter with different σ are shown in Fig.13, in which the AOA's range is from $-100°$ to 100°.

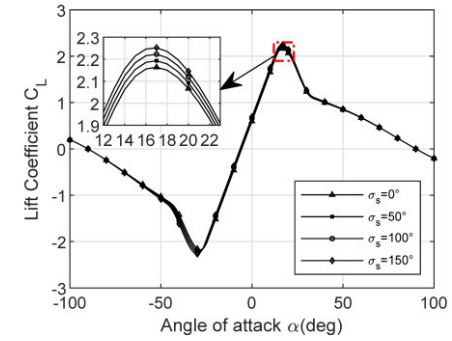

(a) C_L

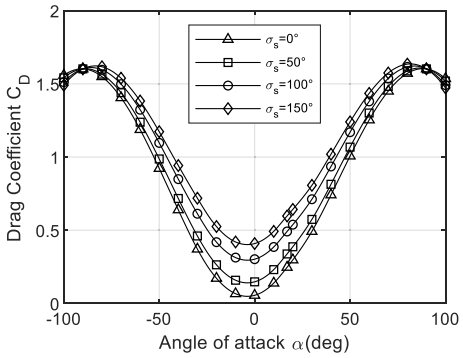

(b) C_D

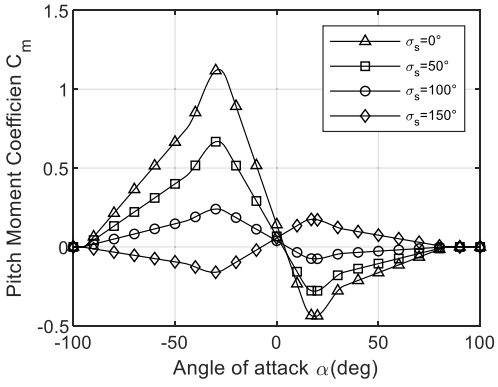

(c) C_{my}

FIGURE 13. Longitudinal aerodynamics with a wide range of angle of attack.

The aerodynamic characteristics of the control surfaces are described in a linear form. Along with the rotating of the rear fuselages, the distance between the elevator and center

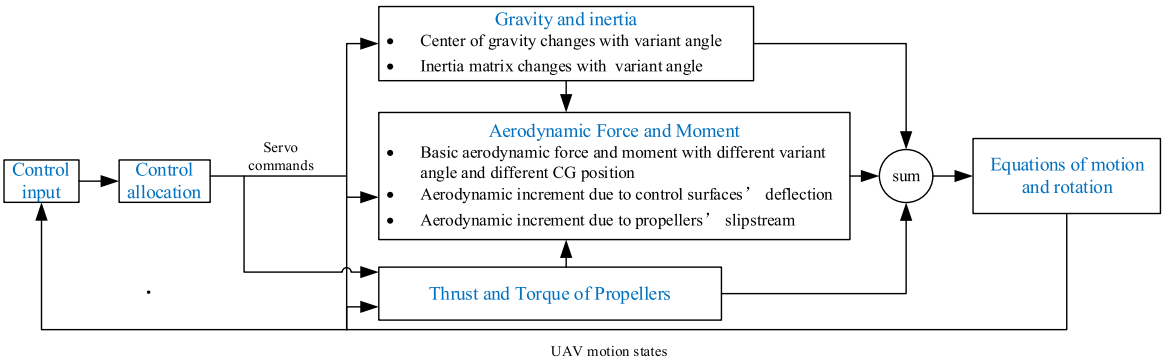

FIGURE 14. Block diagram of the novel tail-sitter's dynamics.

of gravity is changed as shown in Fig.4. It is also the same for the two rudders. The dynamic terms are also added to the aerodynamic model in linear form. Therefore, the complete aerodynamic forces and moments of the tail-sitter are given by

$$\begin{aligned}
L &= \frac{1}{2}\rho V^2 S_{ref}\left(C_L + C_{Lq}\frac{c}{2V}q\right)\\
D &= \frac{1}{2}\rho V^2 S_{ref}\left(C_D + C_{Dq}\frac{c}{2V}q\right)\\
C &= \frac{1}{2}\rho V^2 S_{ref}\left(C_C + C_{Cp}\frac{b}{2V}p + C_{Cr}\frac{b}{2V}r\right)\\
M_{ax} &= \frac{1}{2}\rho V^2 S_{ref} b\left(C_{mx} + C_{mx\delta_a}\delta_a + C_{mxp}\frac{b}{2V}p\right.\\
&\quad \left. + C_{mxr}\frac{b}{2V}r\right)\\
M_{ay} &= \frac{1}{2}\rho V^2 S_{ref}\bar{c}\left(C_{my} + C_{my\delta_e}\delta_e\frac{\cos(\sigma+\vartheta)}{\cos(\vartheta)}\right.\\
&\quad \left. + C_{myq}\frac{c}{2V}q\right)\\
M_{az} &= \frac{1}{2}\rho V^2 S_{ref} b\left(C_{mz} + C_{mz\delta_r}\delta_r\frac{\cos(\sigma+\vartheta)}{\cos(\vartheta)}\right.\\
&\quad \left. + C_{mzp}\frac{b}{2V}p + C_{mzr}\frac{b}{2V}r\right)
\end{aligned} \tag{12}$$

Here, $\delta_e, \delta_a, \delta_r$ are the deflection angles of the elevator, ailerons and rudders respectively. The corresponding control effective coefficients are $C_{my\delta_e}$, $C_{mz\delta_a}$, $C_{mx\delta_r}$. ϑ is shown as Fig.4. The ratio $\cos(\sigma+\vartheta)/\cos(\vartheta)$ reflects the varying fuselage shape' influences on the control effectiveness of elevator and rudders.

E. DYNAMICS MODEL

The dynamic structure of the studied vehicle is shown as Fig.14.

1) MOTIONAL DYNAMICS

External forces and moments acting on the UAV include gravity, aerodynamic forces and moments, propellers' thrust and torques. The gyroscopic torque generated by the rotation of the motors and propellers is ignored.

Motional dynamics equations expressed in the inertial coordinate frame is given as (13).

$$\begin{aligned}
F_{xe} &= m\dot{V}_{ex}\\
F_{ye} &= m\dot{V}_{ey}\\
F_{ze} &= m\dot{V}_{ez}
\end{aligned} \tag{13}$$

External forces expressed in the inertial coordinate frame are given by

$$\begin{bmatrix} F_{xe}\\ F_{ye}\\ F_{ze}\end{bmatrix} = \mathbf{R_{eb}}\begin{bmatrix}\sum_{i=1}^{4} T_i\\ 0\\ 0\end{bmatrix} + \mathbf{R_{eb}}\mathbf{R_{ba}}\begin{bmatrix}-D\\ C\\ -L\end{bmatrix} + \begin{bmatrix}0\\ 0\\ mg\end{bmatrix} \tag{14}$$

2) ROTATIONAL DYNAMICS

The vehicle rotational dynamics is given by

$$\mathbf{M} = \frac{\mathbf{d}}{\mathbf{dt}}(\mathbf{I}\boldsymbol{\omega})$$

According to the Coriolis equation, the above rotational dynamics formula can be expanded as

$$\mathbf{M_b} = \mathbf{I}\dot{\boldsymbol{\omega}}_\mathbf{b} + \boldsymbol{\omega}_\mathbf{b} \times (\mathbf{I}\boldsymbol{\omega}_\mathbf{b}) + \mathbf{I}\dot{\boldsymbol{\omega}}_\mathbf{b}$$

Rewrite it in body coordinate frame, we can get

$$\begin{aligned}
M_{xb} &= I_{xx}\dot{p} + \left(I_{zz} - I_{yy}\right)qr + \dot{I}_{xx}p\\
M_{yb} &= I_{yy}\dot{q} + \left(I_{xx} - I_{zz}\right)pr + \dot{I}_{yy}q\\
M_{zb} &= I_{zz}\dot{r} + \left(I_{yy} - I_{xx}\right)pq + \dot{I}_{zz}r
\end{aligned} \tag{15}$$

Here, $\left[M_{xb}, M_{yb}, M_{zb}\right]^T$ are all the external torques in the body axes. $[p, q, r]^T$ denote the body's rotational angular velocities. The rotation of rear fuselage parts changes the distribution of the vehicle's weight during transition flight, leading to the nonzero derivatives of moments of inertia.

They are calculated by

$$\dot{I} = \begin{bmatrix} \sum_{i=1}^{3} iX_i\sigma^{i-1} & 0 & 0 \\ 0 & \sum_{i=1}^{3} iY_i\sigma^{i-1} & 0 \\ 0 & 0 & \sum_{i=1}^{3} iZ_i\sigma^{i-1} \end{bmatrix} \frac{d\sigma}{dt} \quad (16)$$

External torques in the body axes are given by

$$\begin{aligned} M_{xb} &= Q_1 - Q_2 + Q_3 - Q_4 + M_{xa} \\ M_{yb} &= (T_1 - T_3)\, L_{long} \sin\left(\frac{\sigma}{2} + \vartheta\right) + M_{ya} \\ M_{zb} &= (T_4 - T_2)\, L_{lat} + M_{za} \end{aligned} \quad (17)$$

Here, $L_{long} sin\,(\sigma/2 + \vartheta)$ represents the control arm of tail-mounted propellers, while L_{lat} represents the control arm of P2 and P4 propellers (shown in Fig.4). Combining (12) and (15)-(17), the tail-sitter's rotational dynamic equations are generated and shown as (18).

$$\begin{aligned} M_{ax} &+ \sum_{i=1}^{4} \left\{ (-1)^{i+1}\, \rho n_i^2 D_p^5 \left[B_0 + B_1 \left(\frac{V_\perp}{n_i D_p} \right) \right.\right. \\ &\left.\left. + B_2 \left(\frac{V_\perp}{n_i D_p} \right)^2 \right] \right\} \\ &= I_{xx}\dot{p} + \left(I_{zz} - I_{yy}\right) qr + \dot{I}_{xx} p \\ M_{ay} &+ \left\{ \rho n_1^2 D_p^4 \left[A_0 + A_1 \left(\frac{V_\perp}{n_1 D_p} \right) + A_2 \left(\frac{V_\perp}{n_1 D_p} \right)^2 \right] \right. \\ &- \rho n_3^2 D_p^4 \left. \left[A_0 + A_1 \left(\frac{V_\perp}{n_3 D_p} \right) + A_2 \left(\frac{V_\perp}{n_3 D_p} \right)^2 \right] \right\} L_{long} \\ &\times \sin\left(\frac{\sigma}{2} + \vartheta\right) = I_{yy}\dot{q} + (I_{xx} - I_{zz})\, pr + \dot{I}_{yy} q \\ M_{az} &+ \left\{ -\rho n_2^2 D_p^4 \left[A_0 + A_1 \left(\frac{V_\perp}{n_2 D_p} \right) + A_2 \left(\frac{V_\perp}{n_2 D_p} \right)^2 \right] \right. \\ &+ \rho n_4^2 D_p^4 \left. \left[A_0 + A_1 \left(\frac{V_\perp}{n_4 D_p} \right) + A_2 \left(\frac{V_\perp}{n_4 D_p} \right)^2 \right] \right\} L_{lat} \\ &= I_{zz}\dot{r} + \left(I_{yy} - I_{xx}\right) pq + \dot{I}_{zz} r \end{aligned} \quad (18)$$

IV. CONTROLLER DESIGN

A. CONTROL ALLOCATION

The control inputs involved in the studied tail-sitter include aerodynamic control surfaces' deflections $[\delta_a, \delta_e, \delta_r]^T$ and the rotation speed of each motor $[n_1, n_2, n_3, n_4]^T$. Every control surface's dynamics is treated as a one-order transfer function with time constant equaling 0.05s. Obviously the vehicle's longitudinal motion is an over-actuated control system because number of control inputs is larger than that of states. In order to ensure that a unique controller can be obtained, the following control allocation between the control surfaces' deflection and the motors' rotation speed is given by

$$\begin{aligned} \delta_e &= \frac{k_e k_s}{k_n k_c} (n_1 - n_3) \\ \delta_a &= \frac{k_a k_s}{k_n k_c} (n_1 - n_2 + n_3 - n_4) \\ \delta_r &= \frac{k_r k_s}{k_n k_c} (-n_2 + n_4) \end{aligned} \quad (19)$$

Here, $k_e = -1, k_a = -0.5, k_r = -1$ and they are gains for three rotation channels, $k_c = 0.3$ and represents the proportion of the motor command used for attitude control, $k_s = 0.349 rad$ and represents the maximum of control surfaces' deflection.

B. INCREMENTAL DYNAMIC INVERSION METHOD

The general form of the non-affine, nonlinear system is

$$\begin{aligned} \dot{\mathbf{x}}(t) &= f(\mathbf{x}(t)) + g(\mathbf{x}(t), \mathbf{u}(t)) \\ \mathbf{y}(t) &= h(\mathbf{x}(t)) \end{aligned} \quad (20)$$

where, $\boldsymbol{x}(t)$ is the state vector, $\boldsymbol{u}(t)$ is the control vector, and $\boldsymbol{y}(t)$ is the output vector.

Perform Taylor expansion on (16) at $\boldsymbol{x_0}, \boldsymbol{u_0}$, we can get

$$\begin{aligned} \dot{\mathbf{x}} &= \dot{\mathbf{x}}_0 + \frac{\partial f(\mathbf{x}, \mathbf{u})}{\partial \mathbf{x}}|_{\mathbf{x}_0, \mathbf{u}_0} (\mathbf{x} - \mathbf{x}_0) + \frac{\partial g(\mathbf{x}, \mathbf{u})}{\partial \mathbf{x}}|_{\mathbf{x}_0, \mathbf{u}_0} (\mathbf{x} - \mathbf{x}_0) \\ &\quad + \frac{\partial g(\mathbf{x}, \mathbf{u})}{\partial \mathbf{u}}|_{\mathbf{x}_0, \mathbf{u}_0} (\mathbf{u} - \mathbf{u}_0) + \Delta \\ \dot{\mathbf{y}} &= \frac{dh}{d\mathbf{x}} \dot{\mathbf{x}} \end{aligned} \quad (21)$$

Considering that within a very small sampling time interval, the input response of the system is much faster than the state response, so the contribution of $\Delta\mathbf{x}$ on the output derivative is negligible compared to $\boldsymbol{\Delta u}$. Therefore, (17) can be simplified as

$$\begin{aligned} \dot{\mathbf{y}} &\approx \frac{dh}{d\mathbf{x}} \left[\dot{\mathbf{x}}_0 + \frac{\partial g(\mathbf{x}, \mathbf{u})}{\partial \mathbf{u}}|_{\mathbf{x}_0, \mathbf{u}_0} (\mathbf{u} - \mathbf{u}_0) \right] \\ &= \dot{\mathbf{y}}_0 + B(\mathbf{x}_0, \mathbf{u}_0) \Delta\mathbf{u} \end{aligned} \quad (22)$$

The INDI control law is given by inversing (17)

$$\begin{aligned} \Delta\mathbf{u} &= \mathbf{B}^{-1} (\mathbf{x}_0, \mathbf{u}_0) (\dot{\mathbf{y}}_{des} - \dot{\mathbf{y}}_0) \\ &= \mathbf{u}_0 + \Delta\mathbf{u} \end{aligned} \quad (23)$$

where $\mathbf{y_{des}}$ is the desired output vector, $\mathbf{y}_0$ is the current output vector, $\boldsymbol{B}^{-1}(\boldsymbol{x}_0, \boldsymbol{u}_0)$ is the generalized inverse of current control effectiveness matrix.

C. ATTITUDE CONTROL BASED ON INDI

1) OUTER LOOP CONTROLLER

The desired rate of Euler angles satisfies the following control law.

$$\begin{aligned} \left(\dot{\phi} - \dot{\phi}_{des}\right) + K_{p\phi} (\phi - \phi_{des}) &= 0 \\ \left(\dot{\theta} - \dot{\theta}_{des}\right) + K_{p\theta} (\theta - \theta_{des}) &= 0 \\ \left(\dot{\psi} - \dot{\psi}_{des}\right) + K_{p\psi} (\psi - \psi_{des}) &= 0 \end{aligned} \quad (24)$$

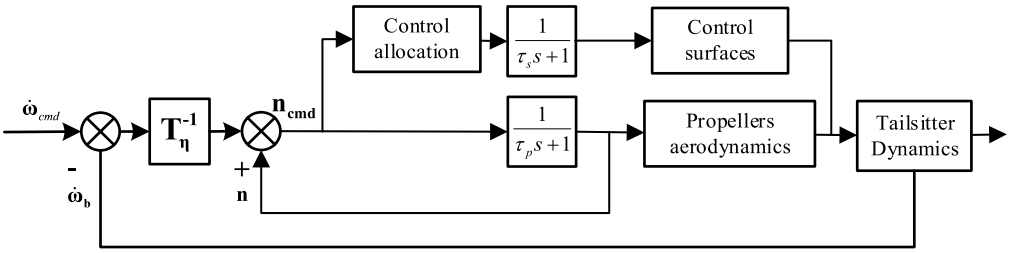

FIGURE 15. Angular velocity controller structure based on INDI.

Here, ψ_{des} is directly given, and ϕ_{des}, θ_{des} are obtained from the altitude controller in the section IV. The desired Euler angular velocity can be obtained by solving the above equation. They are then converted to desired body angular rates $\begin{bmatrix} p_d & q_d & r_d \end{bmatrix}^T$ by

$$\begin{bmatrix} p_d \\ q_d \\ r_d \end{bmatrix} = T_\eta^{-1} \begin{bmatrix} \dot{\phi}_{des} \\ \dot{\theta}_{des} \\ \dot{\psi}_{des} \end{bmatrix} \tag{25}$$

Similarly, the control law for the body angular velocity is given by

$$\begin{aligned} (\dot{p} - \dot{p}_{des}) + K_{pp}(p - p_{des}) &= 0 \\ (\dot{q} - \dot{q}_{des}) + K_{pq}(q - q_{des}) &= 0 \\ (\dot{r} - \dot{r}_{des}) + K_{pr}(r - r_{des}) &= 0 \end{aligned} \tag{26}$$

2) INDI BASED INNER LOOP CONTROLLER

Substituting (19) to (18), we can get

$$\dot{\boldsymbol{\omega}}_{\mathbf{b}} = \mathbf{I}^{-1}(\mathbf{E}\mathbf{n} \circ \mathbf{n} + \mathbf{F}\mathbf{n} + \mathbf{H}) \tag{27}$$

where

$$\mathbf{n} = \begin{bmatrix} n_1 & n_2 & n_3 & n_4 \end{bmatrix}^T$$

$$\mathbf{E} = \rho D_p^4 \begin{bmatrix} D_p B_0 & -D_p B_0 & D_p B_0 & -D_p B_0 \\ A_0 L_{long} \sin\left(\frac{\sigma_s}{2} + \vartheta\right) & 0 & -A_0 L_{long} \sin\left(\frac{\sigma_s}{2} + \vartheta\right) & 0 \\ 0 & -A_0 L_{lat} & 0 & A_0 L_{lat} \end{bmatrix}$$

$$\mathbf{F} = \begin{bmatrix} f_1 & -f_1 & f_1 & -f_1 \\ f_2 & 0 & f_2 & 0 \\ 0 & -f_3 & 0 & f_3 \end{bmatrix}$$

$$\mathbf{H} = \begin{bmatrix} M_{x0}(\beta, \sigma_s, V) - (I_{zz} - I_{yy}) qr - \dot{I}_{xx} p \\ M_{y0}(\alpha, \sigma_s, V) - (I_{xx} - I_{zz}) pr - \dot{I}_{yy} q \\ M_{z0}(\beta, \sigma_s, V) - (I_{yy} - I_{xx}) pq - \dot{I}_{zz} r \end{bmatrix}$$

Inside the matrix $\mathbf{F}$,

$$f_1 = \rho D_p^4 B_1 V_\perp + \frac{\rho V^2 S_{ref} C_{mx\delta_a} b k_a k_s}{2 k_n k_c}$$

$$f_2 = \rho D_p^3 A_1 V_\perp L_{long} \sin\left(\frac{\sigma_s}{2} + \vartheta\right) + \frac{\rho V^2 S_{ref} C_{my\delta_e} \delta_e k_e k_s}{2 k_n k_c} \frac{\cos(\sigma_s/2 + \vartheta)}{\cos(\vartheta)}$$

$$f_3 = \rho D_p^3 A_1 V_\perp L_{lat} + \frac{\rho V^2 S_{ref} C_{mz\delta_r} \delta_r b k_r k_s}{2 k_n k_c} \frac{\cos(\sigma_s/2 + \vartheta)}{\cos(\vartheta)}$$

Referring to (17), replace $\mathbf{y}$ with $\boldsymbol{\omega}_{\mathbf{b}}$ and performing the Taylor expansion, we can get

$$\dot{\mathbf{y}} = \dot{\boldsymbol{\omega}}_{\mathbf{b}} \approx \dot{\boldsymbol{\omega}}_{\mathbf{b0}} + \mathbf{I}^{-1}[2\mathbf{E}diag(n_{10}, \ldots, n_{40}) + \mathbf{F}](\mathbf{n} - \mathbf{n_0}) \tag{28}$$

Here, $\mathbf{n_0}$ is the motor rotation speed at the current time, and $\dot{\boldsymbol{\omega}}_{\mathbf{b0}}$ is the current body angular acceleration. The angular acceleration can be measured by deriving it from the gyroscope measurement [31].

Replace $\dot{\boldsymbol{\omega}}_{\boldsymbol{b}}$ with $\dot{\boldsymbol{\omega}}_{\boldsymbol{cmd}}$, the control law of angular velocity based on INDI is given by

$$\mathbf{n} = [2\mathbf{E}diag(n_{10}, \ldots, n_{40}) + \mathbf{F}]^{-1} \mathbf{I}(\dot{\boldsymbol{\omega}}_{\mathbf{cmd}} - \dot{\boldsymbol{\omega}}_{\mathbf{b0}}) + \mathbf{n_0} \tag{29}$$

Combined with the following total thrust equation, each motor's desired rotation speed can be solved. Total thrust is obtained from the altitude controller as same as the required Euler angles.

$$T_{cmd} = \rho D_p^4 \sum_{i=1}^{4} \left[A_2 \left(\frac{V_\perp}{n_i D_p} \right)^2 + A_1 \left(\frac{V_\perp}{n_i D_p} \right) + A_0 \right] \tag{30}$$

It is noted that the derivatives of moments of inertia are eliminated naturally here, which are much slower than the control inputs.

The block diagram of the attitude angular velocity control based on INDI is shown in Fig.15, in which $\tau_p = 0.05s$ and $\tau_s = 0.05s$.

D. ALTITUDE CONTROL

Simplifying the combination of (13) and (14), the motion dynamic equations of the vehicle are given by

$$T\cos\theta - D\cos(\theta - \alpha) - L\sin(\theta - \alpha) = m\dot{V}_{ex} \tag{31}$$

$$mg - T\sin\theta + D\sin(\theta - \alpha) - L\cos(\theta - \alpha) = m\dot{V}_{zx} \tag{32}$$

Use PD controller to control the altitude

$$\dot{V}_{ezd} = K_{dz}\left(K_{pz}(z_{ed} - z_e) - V_z\right) \tag{33}$$

Substituting (20) to (21), we can get

$$T_d = \frac{-\left(m\dot{V}_{ezd} + L\cos(\theta - \alpha) - D\sin(\theta - \alpha) - mg\right)}{\sin\theta} \tag{34}$$

When the tail-sitter is flying with constant altitude during the transition phase with small disturbance, the angle of attack is equal to the pitch angle, i.e. $\alpha \approx \theta$. Therefore, the altitude controller is rewritten as

$$T_d \approx \frac{-\left(m\dot{V}_{ezd} + L - mg\right)}{\sin\theta} \tag{35}$$

Lift can be estimated from the current ground speed and pitch angle under no disturbance flight condition because it is much easier to read the ground speed and pitch angle from sensors than the airspeed and angle of attack.

V. SIMULATION AND VALIDATION

This part conducts many simulations on the proposed tail-sitter to verify its transition flight capability and the controller's effectiveness.

The control gains are selected as Table 2.

TABLE 2. Attitude control loop gains selection.

Attitude control gains	$K_{p\phi}$	$K_{p\theta}$	$K_{p\psi}$	K_{pp}	K_{pq}	K_{pr}
Value	2	2	2	8	10	8
Altitude control gains	K_{px}	K_{py}	K_{pz}			
Value	1	1	4			

An altitude hold transition strategy is given by

$$\theta_{cmd} = \begin{cases} \theta_0 & t < t_0 \\ \dfrac{\theta_1 - \theta_0}{t_1 - t_0}(t - t_0) + \theta_0 & t_0 \le t < t_1 \\ \theta_1 & t \ge t_1 \end{cases} \tag{36}$$

$$z_{ed} = -h_{cmd} = -h_0 \tag{37}$$

Meanwhile, roll and yaw angle are controlled to 0° during the transition flight. The strategy parameters of the front and back transition flight are set as Table 3.

TABLE 3. Transition flight simulation parameters.

Parameters	θ_0	θ_1	t_0	t_1	h_0
Forward transition	86°	8°	1s	6s	10m
Back transition	8°	86°	56s	61s	10m

According to Table.3, the pitch angle linearly decreases from 86° to 8° during the forward transition and vice versa for the back transition. Altitude is commanded to hold 10 meters all the time. The duration of the front and back transition are both designed as 5 seconds.

The angle between the two rear fuselage's parts needs to be changed according to certain strategy during transition flight. Pitch angle is one of the key factors for judging the flight mode of the tail-sitter. Therefore, the varying angle can be controlled according to the pitch angle. To be specific, a linear varying strategy along with pitch angle is designed as

$$\sigma\left(^\circ\right) = \begin{cases} 0 & \theta < \theta_2 \\ \dfrac{150\left(\theta - \theta_2\right)}{\theta_3 - \theta_2} & \theta_2 \le V < \theta_3 \\ 150 & \theta \ge \theta_3 \end{cases} \tag{38}$$

where $\theta_2 = 70°, \theta_3 = 20°$.

A. NOMINAL CONDITION

Fig.16—Fig.18 show the simulation results of the forward transition flight under no disturbance condition. It can be seen that the pitch angle follows the command smoothly with an acceptable delay which is about 0.25 second. Small fluctuations occur for the roll and yaw angle, whose magnitude are less than 0.43° and 0.21°. They both occur nearly in the end of the forward transition. The altitude decreases by 0.055m at the beginning and returns to 10.0m when the forward transition is completed. As for the velocity, it increases from 4.5m/s to 18.3m/s rapidly within the first four seconds. Then the

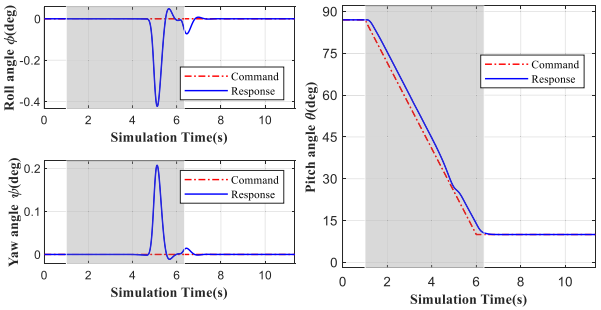

FIGURE 16. Euler angles' response during forward transition flight.

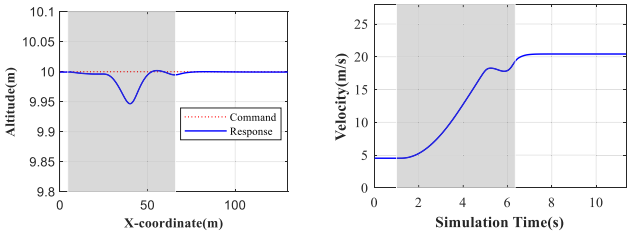

FIGURE 17. Altitude and velocity curves during forward transition flight.

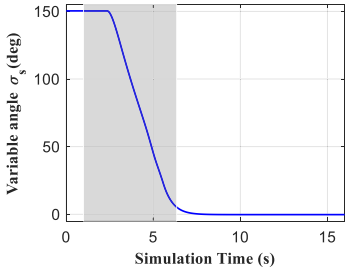

FIGURE 18. Varying angle during forward transition.

velocity decreases by about 0.5m/s from 5.2s to 5.9s. Finally, the velocity increases again to 20.4m/s. This oscillation of velocity is caused by strong nonlinear aerodynamics around the stall angle of attack. The varying angle response is shown as Fig.18.

The varying angle's change during the forward transition is

Under nominal condition, the simulation results of the back transition are shown in Fig.19-Fig.21. In this process, the pitch angle can follow the command smoothly with a delay about 0.25s as same as that of forward transition. What is different from the forward transition is that there is small oscillation at about 57s for the pitch angle, which is caused by the nonlinear aerodynamic pitch moment. The roll angle's maximum fluctuation is 3.24°, and that of yaw angle is 0.92°, both arising in the early stage of back transition flight. They are larger than those during the forward transition. The altitude fluctuates with an amplitude of 0.025m and returns to 10.0m finally. Similarly, there is also an oscillation for the velocity around the stall angle of attack. On the whole, the novel tail-sitter complete the forward and transition flight successfully, which validates the practicality of the vehicle design and the INDI based controller's effectiveness under nominal condition.

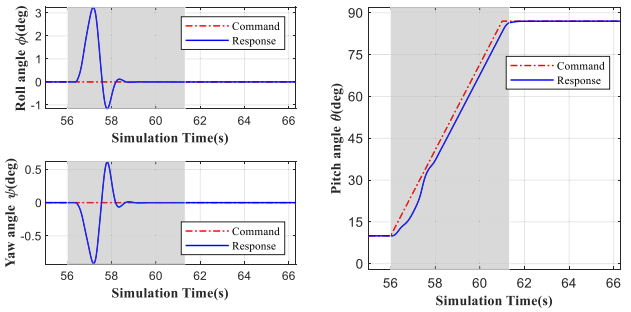

FIGURE 19. Euler angles' response during back transition flight.

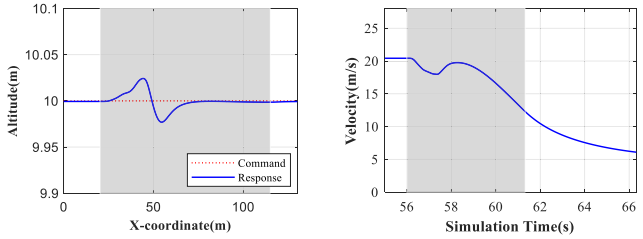

FIGURE 20. Altitude response during the back transition flight.

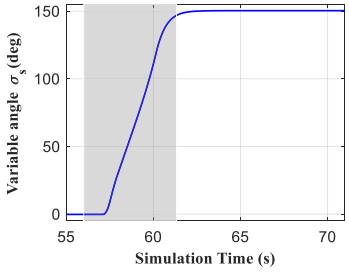

FIGURE 21. Varying angle during back transition.

B. MODEL MISMATCH ANALYSIS

One of the major uncertainties in the transition flight simulation is the high angle of attack aerodynamics, which could not be calculated precisely until now. Specifically, the stall angle of attack prediction is still a difficult problem and there always exists oscillation on the aerodynamics at high angle of attack. Therefore, we firstly simulate the forward and back transition flight with different stall angles of attacks. Then, each aerodynamic coefficient is multiplied by a cosine function with 0.3 magnitude and 1Hz frequency to simulate the oscillated aerodynamics. Note that the change in aerodynamics is not known for the designed controller. Longitudinal aerodynamics being estimated by ground speed and pitch angle is still used for the transition flight control.

The transition flight simulation with different stall angles of attack are shown as Fig.22.

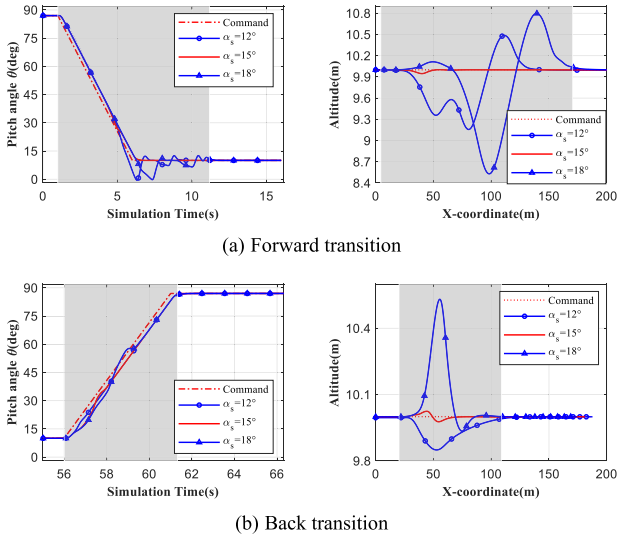

FIGURE 22. Back transition flight with different stall angles of attack.

For this tail-sitter, when the stall angle of attack increases or decreases by 3°, the pitch angle's response becomes less stable than before. The velocity and altitude also come cross larger fluctuations. For example, the altitude's maximum error is −1.5m during the forward transition flight when the stall angle of attack changes to 18°. However, the tail-sitter with designed controller still can complete transition flight with all different stall angles of attack.

Simulation results with aerodynamic coefficients mismatch are shown in Fig.23.

It can be seen that aerodynamic coefficients' mismatch does not have large influence on the transition flight. As far as the pitch angle is concerned, there are more small fluctuations only when the tail-sitter is near to horizontal flight mode. During the forward transition flight, the altitude has more oscillations than the nominal condition. But the maximum

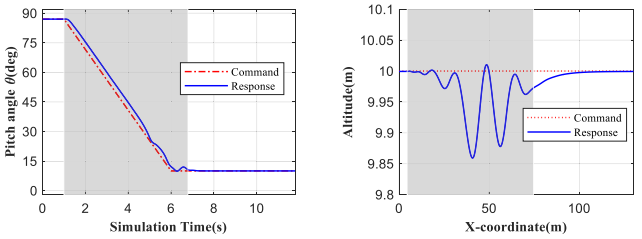

(a) Forward transition

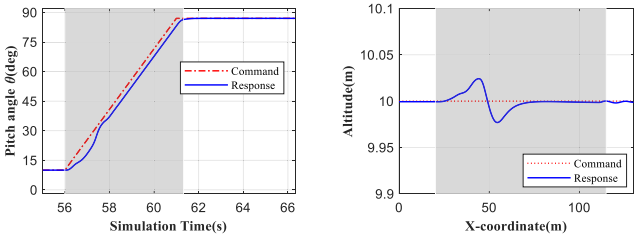

(b) Back transition

FIGURE 23. Pitch angle and altitude response with aerodynamic coefficients mismatch.

magnitude of oscillations is less than 0.15m, which has little influence on the flight safety. As for the back transition flight, the changes brought by coefficients' mismatch can even be ignored compared to the nominal flight condition.

C. VARYING STRATEGIES

In addition to controlling the rear fuselages' varying angle according to the pitch angle, we also proposed two other varying strategies.

Varying strategy 1 is given by

$$\sigma\left(^{\circ}\right)=\begin{cases}150 & V<V_1\\ \dfrac{-150\left(V-V_1\right)}{V_2-V_1}+150 & V_1\le V<V_2\\ 0 & V\ge V_2\end{cases}\tag{39}$$

Varying strategy 2 is given by

$$\sigma=75^{\circ}\tag{40}$$

The first strategy is to control the varying angle according to the flight speed. During the transition flight, when the speed is less than $V_1=4m/s$, the two rear fuselage's parts are fully separated to 150° and the tail-mounted propellers can provide maximum pitch moment. When the speed is larger than $V_2=18m/s$, the two rear fuselages are completely combined, turning the tail sitter to a conventional fixed-wing UAV with a streamlined geometry, and the longitudinal control turns to rely on the deflection of the elevator. Between these two speed limits, the varying angle changes linearly according to flight velocity.

The meaning of the second varying strategy is keeping varying angle holding at 75° during the transition flight, with the variation between 75° and 150° being carried out in the vertical flight mode and the variation between 0° and 75° in the horizontal flight mode.

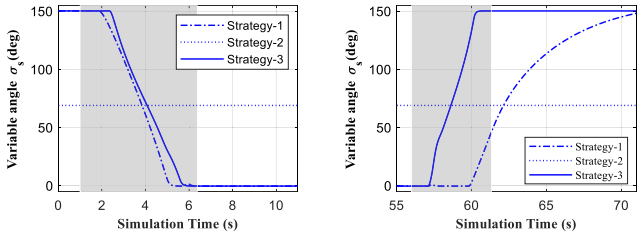

(a) Forward transition flight (b) Back transition flight

FIGURE 24. Varying angle curves with different strategies.

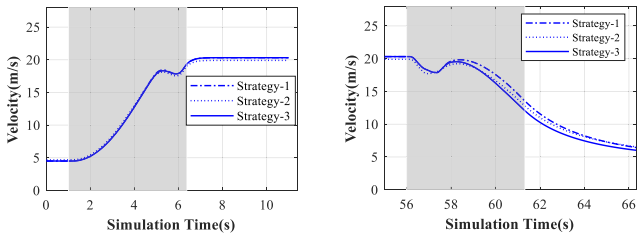

(a) Forward transition flight (b) Back transition flight

FIGURE 25. Velocity curves with different strategies.

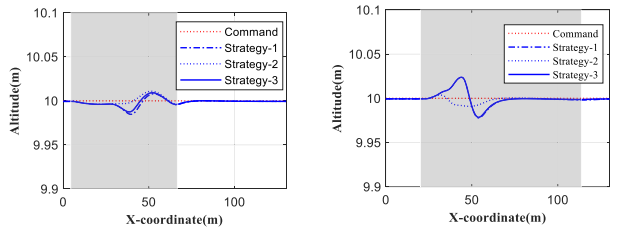

(a) Forward transition flight (b) Back transition flight

FIGURE 26. Velocity curves with different varying strategies.

Denote the linear varying strategy along with pitch angle discussed in the beginning of section IV as strategy 3 and simulate them all, we can get the following results.

The results show that speed-related varying strategy is the most sluggish and uncertain one. Especially for back transition, the varying process is much slower for the velocity-related strategy. As for the altitude, there is no significant difference in it among different strategies. However, the precision of measuring air velocity is much lower than that of pitch angle in reality. Therefore speed-related varying strategy is not the best varying strategy. As for the strategy 2, there is no instinct difference compared to strategy 3, but this strategy extends the varying time, which may bring more uncertainties. In conclusion, strategy 3 which varies the fuselage shape according to the pitch angle is the prior choice for this novel tail sitter.

D. WIND DISTURBANCE CONSIDERATION

Tail-sitter UAV is very sensitive to gusts during transition flight for its large windward wing area. In order to verify the researched tail-sitter's gust resistant ability, the "1-cosine" standard gust model is applied on the transition flight.

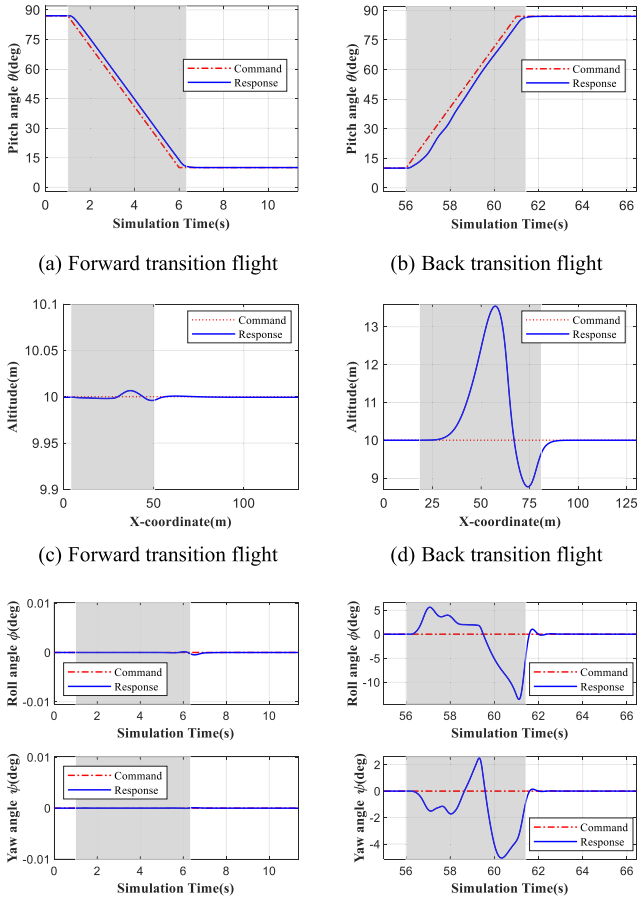

(a) Forward transition flight (b) Back transition flight

(c) Forward transition flight (d) Back transition flight

(e) Forward transition flight (f) Back transition flight

FIGURE 27. **Transition flight simulation with gust disturbance.**

The gust speed is within 5 m/s and unmeasurable for the controller. The direction of applied gust is along the $-x_e$ direction, which means it is almost perpendicular to the wing surface in the early stage of forward transition flight.

From Fig.27, we can see that the gust has little influence on the forward transition flight. The altitude's fluctuation even becomes smaller than those without gust disturbance. But for the back transition flight, the gust disturbance has a great influence. It causes the tail-sitter climbing up to 13.55 meters and then dropping to 8.76 meters. At the same time, the roll and yaw angle also experience larger oscillations than that during forward transition. However, the novel tail-sitter is able to conduct transition flight with gust disturbance successfully.

VI. CONCLUSION

1) This article provided a novel tail-sitter UAV with varying fuselage shape design and validated its transition flight capability through simulation. Further speaking, the practicality of the varying fuselage shape design is verified as well for the successful transition flight.

2) The novelty of this article stems from: a) the design of varying fuselage shape for tail-sitter to enhance the vertical and horizontal flight capability, b) the transition flight modeling and control based on INDI method for the novel tail-sitter never been studied before, c) the comparison between different flight strategies for the fuselage shape's varying motion during transition flight.

3) Nominal and model mismatch simulations validate the effectiveness of INDI based control method. Besides, transition flight with gust disturbance is simulated, verifying the controller's robustness as well. Compared with nominal conditions, the gust has little influence on the forward transition flight. For the back transition flight, the gust causes an decrease about 1.24m in altitude, which is not a big problem for successful transition maneuver.

4) Three different varying strategies for the fuselage shape's varying were simulated and compared. It is concluded that the strategy related to the pitch angle is a prior choice for its accuracy and reliability.

REFERENCES

[1] V. Kumar and N. Michael, "Opportunities and challenges with autonomous micro aerial vehicles," *Int. J. Robot. Res.*, vol. 31, no. 11, pp. 1279–1291, Aug. 2012.

[2] S. Watkins, J. Burry, A. Mohamed, M. Marino, S. Prudden, A. Fisher, N. Kloet, T. Jakobi, and R. Clothier, "Ten questions concerning the use of drones in urban environments," *Building Environ.*, vol. 167, Jan. 2020, Art. no. 106458.

[3] A. S. Saeed, A. B. Younes, S. Islam, J. Dias, L. Seneviratne, and G. Cai, "A review on the platform design, dynamic modeling and control of hybrid UAVs," in *Proc. Int. Conf. Unmanned Aircr. Syst. (ICUAS)*, Jun. 2015, pp. 806–815.

[4] S. Zhang, "Review of vertical take-off and landing aircraft," in *Proc. 2nd Int. Conf. Mech., Control Comput. Eng. (ICMCCE)*, Dec. 2017, pp. 53–56.

[5] W. Liu, G. He, H. Yu, T. Li, and J. Zhang, "Review on dynamic modeling of tilt-rotor UAVs in low speed flight," in *Proc. Int. Conf. Sens., Diagnostics, Prognostics, Control (SDPC)*, Aug. 2018, pp. 284–290.

[6] N. T. Hegde, V. I. George, C. G. Nayak, and K. Kumar, "Design, dynamic modelling and control of tilt-rotor UAVs: A review," *Int. J. Intell. Unmanned Syst.*, vol. 8, no. 3, pp. 143–161, Aug. 2019.

[7] B. Wang, Z.-X. Hou, Y.-F. Lu, and X.-F. Zhu, "Hover performance estimation and validation of battery powered vertical takeoff and landing aircraft," *J. Central South Univ.*, vol. 23, no. 10, pp. 2595–2603, Oct. 2016.

[8] A. S. Saeed, A. B. Younes, C. Cai, and G. Cai, "A survey of hybrid unmanned aerial vehicles," *Progr. Aerosp. Sci.*, vol. 98, pp. 91–105, Apr. 2018.

[9] M. Kondratiuk and L. Ambroziak, "Design and dynamics of kinetic launcher for unmanned aerial vehicles," *Appl. Sci.*, vol. 10, no. 8, p. 2949, Apr. 2020.

[10] R. H. Stone, "The T-wing tail-sitter unmanned air vehicle: From design concept to research flight vehicle," *Proc. Inst. Mech. Eng., G, J. Aerosp. Eng.*, vol. 218, no. 6, pp. 417–433, Jun. 2004.

[11] R. D. Fisher. (2016). *China Reveals Data on Vd200 Flying-Wing VTUAV*. [Online]. Available: http://www.janes.com/article/59105/china-reveals-data-on-vd200-flying-wing-vtuav

[12] Y. Yang, X. Wang, J. Zhu, X. Yuan, and X. Zhang, "Robust proportional incremental nonlinear dynamic inversion control of a flying-wing tailsitter," *Proc. Inst. Mech. Eng., G, J. Aerosp. Eng.*, vol. 234, no. 16, pp. 2274–2295, May 2020.

[13] *ATMOS UAV*. Accessed: Feb. 20, 2021. [Online]. Available: https://www.atmosuav.com/

[14] M. Hochstenbach, C. Notteboom, B. Theys, and J. De Schutter, "Design and control of an unmanned aerial vehicle for autonomous parcel delivery with transition from vertical take-off to forward flight–VertiKUL, a quadcopter tailsitter," *Int. J. Micro Air Vehicles*, vol. 7, no. 4, pp. 395–405, Dec. 2015.

[15] K. Bramsiepe, A. Voß, and T. Klimmek, "Design and sizing of an aeroelastic composite model for a flying wing configuration with maneuver, gust, and landing loads," *CEAS Aeronaut. J.*, vol. 11, no. 3, pp. 677–691, 2020.

[16] S. S. Chauhan and J. R. R. A. Martins, "Tilt-wing eVTOL takeoff trajectory optimization," *J. Aircr.*, vol. 57, no. 1, pp. 93–112, Jan. 2020.
[17] J. L. Tangler and C. Ostowari, "Horizontal axis wind turbine post stall airfoil characteristics synthesization," Wind Energy Res. Center, Tech. Rep. SERI-TP-257-4400, Jun. 1991.
[18] L. Viterna and R. Corrigan, "Fixed pitch rotor performance of large horizontal axis wind turbines," *Large Horiz. Wind Turbines*, vol. 1, pp. 69–85, Jan. 1982.
[19] L. Haixu, Q. Xiangju, and W. Weijun, "Multi-body motion modeling and simulation for tilt rotor aircraft," *Chin. J. Aeronaut.*, vol. 23, no. 4, pp. 415–422, Aug. 2010.
[20] C. Chao, S. Lincheng, Z. Daibing, and Z. Jiyang, "Mathematical modeling and control of a tiltrotor UAV," in *Proc. IEEE Int. Conf. Inf. Autom. (ICIA)*, Aug. 2016, pp. 2016–2021.
[21] J. Zhang, L. Sun, X. Qu, and L. Wang, "Time-varying linear control for tiltrotor aircraft," *Chin. J. Aeronaut.*, vol. 31, no. 4, pp. 632–642, Apr. 2018.
[22] N. Raj, R. Banavar, Abhishek, and M. Kothari, "Attitude control of novel tail sitter: Swiveling Biplane–Quadrotor," *J. Guid., Control, Dyn.*, vol. 43, no. 3, pp. 599–607, Mar. 2020.
[23] Y. Jung and D. H. Shim, "Development and application of controller for transition flight of tail-sitter UAV," *J. Intell. Robotic Syst.*, vol. 65, nos. 1–4, pp. 137–152, Jan. 2012.
[24] T. Matsumoto, K. Kita, R. Suzuki, A. Oosedo, K. Go, Y. Hoshino, A. Konno, and M. Uchiyama, "A hovering control strategy for a tail-sitter VTOL UAV that increases stability against large disturbance," in *Proc. IEEE Int. Conf. Robot. Autom.*, May 2010, pp. 54–59.
[25] P. Casau, D. Cabecinhas, and C. Silvestre, "Autonomous transition flight for a vertical take-off and landing aircraft," in *Proc. IEEE Conf. Decis. Control Eur. Control Conf.*, Dec. 2011, pp. 3974–3979.
[26] R. H. Stone, "Control architecture for a tail-sitter unmanned air vehicle," in *Proc. 5th Asian Control Conf.*, vol. 2, Jul. 2004, pp. 736–744.
[27] P.-R. Bilodeau and F. Wong, "Modeling and control of a hovering mini tail-sitter," *Int. J. Micro Air Vehicles*, vol. 2, no. 4, pp. 211–220, Dec. 2010.
[28] T. Lombaerts, J. Kaneshige, S. Schuet, B. L. Aponso, K. H. Shish, and G. Hardy, "Dynamic inversion based full envelope flight control for an eVTOL vehicle using a unified framework," in *Proc. AIAA Scitech Forum*, 2020, p. 1619.
[29] Z. Liu, J. Guo, M. Li, S. Tang, and X. Wang, "VTOL UAV transition maneuver using incremental nonlinear dynamic inversion," *Int. J. Aerosp. Eng.*, vol. 2018, Nov. 2018, Art. no. 6315856.
[30] G. Di Francesco and M. Mattei, "Modeling and incremental nonlinear dynamic inversion control of a novel unmanned tiltrotor," *J. Aircr.*, vol. 53, no. 1, pp. 73–86, Jan. 2016.
[31] E. J. J. Smeur, M. Bronz, and G. C. H. E. de Croon, "Incremental control and guidance of hybrid aircraft applied to a tailsitter unmanned air vehicle," *J. Guid., Control, Dyn.*, vol. 43, no. 2, pp. 274–287, Feb. 2020.
[32] Y. Yang, J. Zhu, and J. Yang, "INDI-based transitional flight control and stability analysis of a tail-sitter UAV*," in *Proc. IEEE Int. Conf. Syst., Man, Cybern. (SMC)*, Oct. 2020, pp. 1420–1426.

XINGLU XIA received the B.S. degree in aircraft design from Beihang University, Beijing, China, in 2016, where he is currently pursuing the Ph.D. degree with the School of Aeronautic Science and Engineering. His current research interests include new concept aircraft design and eVTOL aircraft design and control.

MUQING YANG received the B.S. and Ph.D. degrees in aircraft design from Beihang University, Beijing, China, in 2008 and 2014, respectively. His current research interests include new concept aircraft design, aircraft optimization, and computational fluid dynamics.

GANG CHEN received the B.S. degree in aircraft design from Beihang University, Beijing, China, in 2015, where he is currently pursuing the Ph.D. degree with the School of Aeronautic Science and Engineering. His current research interests include new concept aircraft design and hybrid power VTOL design and optimization.

LIANG ZHANG received the B.S. degree in aircraft design from Beihang University, Beijing, China, in 2015, where he is currently pursuing the Ph.D. degree with the School of Aeronautic Science and Engineering. His current research interests include new concept aircraft design, solar-powered drone design, and aerodynamic optimization.

JIAJIA HOU received the B.S. degree in automatic control and the M.S. degree in flight control from Beihang University, Beijing, China, in 2016 and 2019, respectively. She is currently working with the Science and Technology on Space Physics Laboratory, Beijing. Her major interests include adaptive control and dynamic inversion control.